Ab initio phonon point defect scattering and thermal transport in graphene

Carlos A. Polanco and Lucas Lindsay

Ab initio phonon point defect scattering and thermal transport in graphene

Carlos A. Polanco and Lucas Lindsay

Materials Science and Technology Division, Oak Ridge National Laboratory, Oak Ridge, Tennessee 37831, USA

Abstract

We study the scattering of phonons from point defects and their effect on lattice thermal conductivity κ using a parameter-free *ab initio* Green's function methodology. Specifically, we focus on the scattering of phonons by Boron (B), Nitrogen (N) and Phosphorus substitutions as well as single- and double-Carbon vacancies in graphene. We show that changes of the atomic structure and harmonic interatomic force constants (IFCs) locally near defects govern the strength and frequency trends of the scattering of out-of-plane acoustic (ZA) phonons, the dominant heat-carriers in graphene. ZA scattering rates due to N substitutions are nearly an order of magnitude smaller than that for B defects despite having similar mass perturbations. Furthermore, ZA phonon scattering rates from N defects decrease with increasing frequency in the lower frequency spectrum in stark contrast to expected trends from simple models. ZA phonon-vacancy scattering rates are found to have a significantly softer frequency dependence ($\sim\omega^0$) in graphene than typically employed in phenomenological models. The rigorous Green's function calculations demonstrate that typical mass defect models do not adequately describe ZA phonon-defect scattering rates. Our *ab initio* calculations capture well the trend of κ vs. vacancy density from experiments, though not the magnitudes. This work elucidates important insights into phonon defect scattering and thermal transport in graphene, and demonstrates the applicability of first principles methods toward describing these properties in imperfect materials.

I. INTRODUCTION

Parameter-free Peierls-Boltzmann transport calculations of thermal conductivity κ have been critical to complementing and building our fundamental understanding of phonon flow through *defect-free* crystalline materials [1–5]. This understanding combined with predictive computation can guide the design of new materials that more efficiently carry or block thermal energy. For instance, new "rules of thumb" relating features of phonon dispersions with intrinsic phonon-phonon scattering has guided the prediction of ultra-high thermal conductivity in cubic BAs [6]. Unfortunately, this prediction has not been validated by experiment [7,8], as synthesized BAs samples contain extended and point defects, which can dramatically alter the phonon scattering landscape [9]. Thus, computational prediction of κ for *real* materials with design of targeted transport properties also requires parameter-free calculation of the scattering of phonons from material imperfections.

Accurately calculating phonon-defect scattering without fitting parameters, i.e. beyond simple models, is a challenging task. Atomic structure and thus the forces pairing atoms near a defect differ from that of the perfect crystal. Furthermore, these features also depend on external variables such as temperature and pressure, and point defects can form clusters and are otherwise randomly distributed within a material. Moreover, controlled synthesis and characterization of defects and their distributions are extremely challenging, and experimental studies linking the effects of defects to thermal transport behavior are generally limited. All these features hinder the benchmarking of advanced theoretical methods with quality measurements and promote the use of simplified models built with fitting parameters to compensate for unknown or neglected features of the fundamental processes governing phonon-defect scattering.

Typical calculations considering phonon-defect scattering employ models developed from first order perturbation theory (Fermi's golden rule or Born approximation) considering only changes in the atomic masses, or effective changes in mass variance to crudely account for force and bond disorder [10–12]. These include simple and popular equations ($1/\tau^d \propto \omega^\delta$, with δ some positive integer) that assume a Debye approximation for phonon dispersions and that rely on an adjustable proportionality constant to fit measured data. More recent work has coupled mass-defect scattering with realistic dispersions and eigenvectors from density functional theory calculations, particularly to describe phonon-isotope scattering rates for predictive transport calculations [13,14], though still within first order perturbation theory.

Errors induced by these various approximations to describe phonon-defect scattering have recently been addressed by parameter-free *ab initio* Green's function calculations [15–17], which are not restricted to small perturbations or low frequency windows. These calculations have demonstrated that simple approximations do not capture well the strength of phonon scattering from clusters of isotopes in graphene [15] or from Si and Ge nanoparticles in $Si_{0.5}Ge_{0.5}$ alloys [16]. Furthermore, Green's function calculations have demonstrated the importance of also considering structural and harmonic interatomic force constants (IFCs are used to denote harmonic interatomic force constants. The few cases when we refer to

anharmonic interatomic force constants (below Eq. 7) are labeled with the 'anharmonic' adjective) variance caused by the presence of defects [9,18,19], which defines a multi-dimensional energy landscape where phonons interfere and scatter. It has been shown that the usual way of modeling phonon-vacancy scattering, which considers the vacancy as a stronger mass defect [11], fails to predict the scattering strength due to vacancies in diamond [18] and BAs [9], even at low frequencies where first order perturbation theory is expected to be reasonable. These results highlight the importance of including defect induced IFC variance in phonon-defect scattering calculations, important for predicting and understanding κ in real materials.

Despite these recent parameter-free theoretical works, our fundamental understanding of and predictive capabilities for determining thermal transport in defected materials is far from complete. We do not have property/transport relationships to describe the effects of large defect-induced perturbations on thermal transport. We lack physical insights on how key defect features affect lattice vibrations and transport; neither do we have simple, yet accurate equations to explain transport phenomena. Similar to thermal transport in perfect crystalline materials, further parameter-free phonon-defect scattering calculations in real materials may elucidate interesting new physics and continue to build our intuition of defect/vibrational coupling phenomena, while providing key material properties toward targeted thermal management applications. In this paper, we present such calculations in a 2D material (graphene) that includes defect induced structural relaxation and mass and force disorder.

We choose graphene as the subject of this theoretical study of phonon-defect scattering and κ because of its technological and scientific significance [20,21], the important correlations made between Raman signals and defect types and concentrations [22,23], and because its 2D nature reduces the computational cost of numerical calculations. We explore variation in κ of graphene by Boron, Nitrogen and Phosphorus substitutions, which are candidates to dope graphene and alter its electronic structure [24,25]. Also, we study the lattice thermal transport response to single-Carbon and double-Carbon vacancies (two adjacent vacancies), which can be generated in a controlled manner by irradiation [23,26]. A significant body of work has been built characterizing defects [27] and separately κ in graphene [28–32], from table-top spectroscopic tools. Of particular importance in the present work is the use of Raman peak intensities to characterize the type and number of defects (e.g. sp^3-defects, vacancies and boundaries) [22,23], and to measure thermal conductivity of defected graphene [26]. This experiment constituted our main motivation to examine phonon-defect scattering in graphene.

This manuscript is organized as follows: After a brief theoretical background (Sec. II), we give the scattering rates obtained from *ab initio* Green's function calculations and compare with first order perturbation approximations (Sec. III and IV). We explore the relationship of IFCs and scattering rates arising from substitutional defects (Sec. III) and vacancies (Sec. IV) and show the change generated on the graphene thermal conductivity due to those defects (Sec. V). In Sec. VI we give concluding remarks.

II.   THEORETICAL BACKGROUND

Consider a propagating phonon whose branch j and momentum $\boldsymbol{q}$ are labeled by λ that scatters via interaction with a defect into another phonon labeled λ'. The average transition rate for this process can be described by a Green's function methodology [16]

$$(1) \quad R_{\lambda \to \lambda'} = \frac{\pi \Omega_\lambda}{\omega_\lambda \Omega} |\langle \lambda|T_d|\lambda'\rangle|^2 \delta\left(\omega_\lambda^2 - \omega_{\lambda'}^2\right)$$

with ω_λ the phonon eigenfrequency, Ω_λ the volume where the eigenstate λ is normalized, Ω the volume of the sample and T_d the so-called T-matrix characterizing the interaction and defined below. Summing Eq. 1 over all final states, using the optical theorem and assuming the scattering of each defect is independent of the others, the phonon-defect scattering rate is given by [15]

$$(2) \quad 1/\tau_\lambda^d = n_d v_\lambda \sigma_\lambda^d = n_d \frac{\Omega_\lambda}{\omega_\lambda} Im\{\langle \lambda|T_d|\lambda\rangle\}$$

with n_d the defect density, v_λ the phonon group velocity and σ_λ^d the defect scattering cross section. We note that the mode subscript λ for the defect scattering rates will be dropped in subsequent discussions. The T-matrix for phonon-defect scattering

$$(3) \quad T_d = [I - V_d G_0]^{-1} V_d$$

is built from the identity matrix I, the perturbation V_d and the retarded Green's function G_0 of the unperturbed system. The perturbation $V_d = H_d - H_0$ captures the differences introduced by a defect in the perfect system. H_d and H_0 are the dynamical matrices ($H = M^{-1/2}KM^{-1/2}$) for the system with and without defects, respectively. M is a diagonal matrix containing the mass of each atom and K is the matrix with the interatomic force constants relating the various atoms. The Green's function is given by $G_0 = [\omega^2 I - H_0 - \Sigma]^{-1}$, with Σ the self-energy. Further details regarding calculation of G_0, including the self-energy term, can be found in [15,33,34]. The T-matrix is also defined as $T_d = V_d + V_d G_0 V_d + V_d G_0 V_d G_0 V_d + \cdots$, which gives rise to Fermi's golden rule when T_d is replaced by its first order perturbation $T_d \approx V_d$ in Eq. 1. This is also referred to as the Born approximation.

The thermal conductivity in the z direction is given by

$$(4) \quad \kappa = \frac{1}{\Omega} \sum_\lambda \hbar \omega_\lambda \frac{\partial N_\lambda}{\partial T} v_{\lambda z}^2 \tau_{\lambda z},$$

with $\hbar \omega_\lambda \frac{\partial N_\lambda}{\partial T}$ the heat capacity per mode, N_λ the Bose-Einstein distribution, T the temperature, $v_{\lambda z}$ the phonon group velocity in the z direction and $\tau_{\lambda z}$ the transport lifetime along the applied temperature gradient in the z direction. The transport lifetime (lifetime in the presence of a temperature gradient [1,35–37]) comes from the self-consistent solution of the linearized form of the BTE, commonly known as the full solution of the BTE. The initial condition for this iterative procedure is built from individual mode-dependent scattering rates combining boundary $1/\tau_\lambda^b = |v_\lambda|/L$ [36], defect $1/\tau_\lambda^d$ and 3-phonon $1/\tau_\lambda^{ph}$ [36,38] scattering using Matthiessen's rule

$$(5) \quad \frac{1}{\tau_\lambda} = \frac{1}{\tau_\lambda^b} + \frac{1}{\tau_\lambda^d} + \frac{1}{\tau_\lambda^{ph}}$$

Replacing this initial condition expression (Eq. 5) for the transport lifetime in Eq. 4 is equivalent to employing the relaxation time approximation, which was shown to give a poor representation of κ in graphene [39–42]. Therefore, the transport lifetimes are determined from full solution of the Peierls-Boltzmann transport equation as described in detail previously [39,40].

For each defect structure, we obtain relevant harmonic IFCs for input into phonon-defect scattering calculations (Eq. 2) by the finite displacement method in relaxed 9×9 supercells. The IFCs from atoms up to the 13th nearest neighbor shell around the defect were then inserted into the central region of a 240-atom rectangular graphene supercell. We enforce the acoustic sum rule on the rectangular supercell by equating the onsite IFC matrix of each atom to the negative of the sum of the IFC matrices of its neighbors, which we refer to as the simple acoustic sum rule. Finally, we use the supercell to define the perturbation V_d and calculate the phonon-defect scattering rates and thermal conductivities as described above. Details of the calculation are spelled out more explicitly in Appendix A.

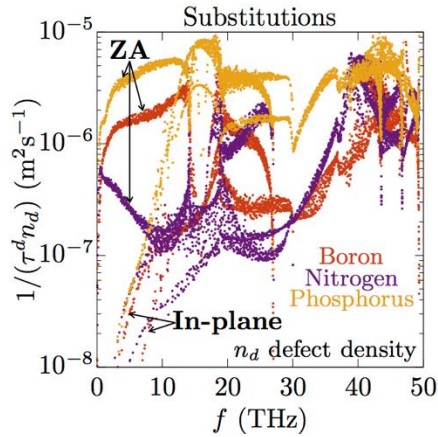### III.　　PHONON-DEFECT SCATTERING BY SUBSTITUTIONS

Figure 1. T-matrix phonon-defect scattering rates $(1/\tau_\lambda^d)$ of graphene with B, N and P substitutions. Note that these scattering rates are scaled to be independent of the arbitrary defect density n_d. As shown, the ZA scattering rates due to N defects are much weaker than those from B and P defects, and decrease with increasing frequency up to 10 THz, unlike in-plane scattering rates and ZA rates for B and P defects.

Using the T-matrix method, we calculate the scattering of phonons in graphene due to Boron, Nitrogen and Phosphorus substitutions (Fig. 1). Three key features to note about these phonon-defect scattering rates are: (i) $\tau^{-1}_{Nitrogen}$ are much weaker than τ^{-1}_{Boron}, (ii) $\tau^{-1}_{Nitrogen}$ for lower frequency ZA modes surprisingly decrease with increasing frequency, and (iii) ZA phonon-defect scattering rates are significantly stronger than those for in-plane modes. Features (i) and (ii) challenge established expectations for the magnitude and frequency dependence of phonon-defect scattering, which are built from first order perturbation theory considering on-site mass or effective mass defect scattering (neglecting IFC variance). According to this approximation, phonon-mass-defect scattering rates for graphene are given by [13,39]

$$(6) \quad \frac{1}{\tau^d_\lambda} = \frac{\pi}{2N_0} \omega^2_\lambda g \sum_{k,\lambda'} \left| e^{\lambda*}_k \cdot e^{\lambda'}_k \right|^2 \delta(\omega_\lambda - \omega_{\lambda'})$$

with $g = \sum_i f_i (1 - m_i/\overline{m})^2$, f_i and m_i the fraction and mass of the ith type of atom, $\overline{m}$ the average mass, and e^λ_k the eigenvector of the kth atom in the unit cell. The fraction of defects is given by $f_d = n_d S_0$, with S_0 the area per Carbon atom, and the fraction of Carbon is given by $f_C = 1 - f_d$. When the defect atom changes only g changes, as intrinsic phonon properties (e.g., frequencies, velocities) change very little for reasonable defect concentrations. Eq. 6 then predicts $\tau^{-1}_{Boron} < \tau^{-1}_{Nitrogen} < \tau^{-1}_{Phosphorous}$. For instance, when $f_d = 1.1\%$, $\tau^{-1}_{Nitrogen} = 2.75\tau^{-1}_{Boron}$ and $\tau^{-1}_P = 241.5\tau^{-1}_B$. On the contrary, the T-matrix calculations in Fig. 1 give $\tau^{-1}_{Nitrogen} < \tau^{-1}_{Boron} < \tau^{-1}_{Phosphorous}$, and the scattering rates of ZA phonons for P defects are only 2.5 times larger than those for B defects, orders of magnitude weaker than from simple predictions. Our calculations also show a surprising decrease of $\tau^{-1}_{Nitrogen}$ with increasing frequency for the ZA phonons at low frequencies. This result contradicts the increasing frequency dependence expected from Eq. 6 that predicts $1/\tau^d \propto \omega^2$ for ZA phonons in this frequency regime [39]. The scattering rates distinguished by polarization are shown in Appendix A Fig. 9.

It has been shown previously that perturbative approaches to describe phonon-defect scattering fail when the IFC variance is large [18]. Nevertheless, we have limited physical insights connecting those changes with the resulting scattering rates. To build a better understanding of phonon-defect scattering from B, N and P substitutional defects we compare T-matrix scattering rates with calculations including changes in defect mass and in IFCs separately (Fig. 2). For B and N defects whose mass perturbation is small, the variation on the IFCs alone dictates the acoustic scattering rates (Figs. 2a and 2b) and not including it underestimates the scattering by up to two orders of magnitude. For P defects whose mass perturbation is larger, the scattering rates of out-of-plane phonons are dictated by IFC variation, while those for in-plane phonons by mass variation (Fig. 2c). In general, the scattering rates of the dominant heat carriers in graphene, ZA phonons, are dictated only by the changes in IFCs (Fig. 2), and simple mass variance models for phonon-defect scattering likely give a poor description of thermal transport in graphene with moderate defect concentrations.
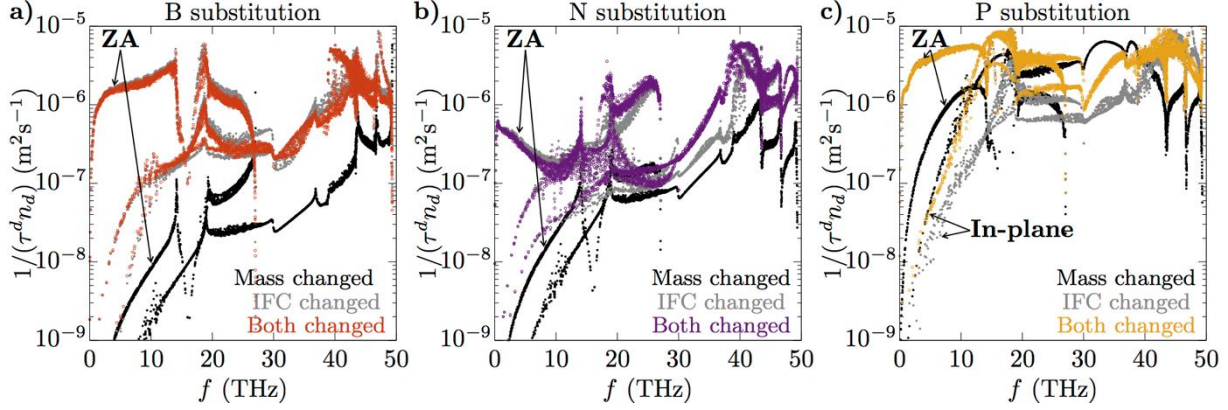
Figure 2. *T*-matrix scattering rates for **a)** Boron, **b)** Nitrogen and **c)** Phosphorous defects comparing when only the defect mass is changed or when only the IFCs are changed with the full calculation. The scattering rates of ZA phonons, which carry most of the heat in graphene, are dictated by IFC variance in all three systems.

Next we focus on B and N defect scattering rates, which despite having similar mass perturbations in graphene, demonstrate qualitative differences. In particular, *T*-matrix calculations give ZA $\tau_{Nitrogen}^{-1}$ that decrease with frequency (1-10 THz range) becoming comparable with in-plane rates (Fig. 2b) (both transverse (TA) and longitudinal (LA)), while ZA τ_{Boron}^{-1} increase with frequency and are at least an order of magnitude larger than the in-plane acoustic rates (Fig. 2a). This is not determined by mass variance, nor do the different density of states for ZA and in-plane modes govern this behavior as these are the same for both N and B defects. Thus, the relative differences of ZA and in-plane scattering rates (smaller for N defects, larger for B defects) for the two systems are derived from relative differences of the in-plane and out-of-plane IFCs. We define ΔK_{op} (ΔK_{ip}) as the percent difference of the out-of-plane (in-plane) IFCs in the defect system with those of the unperturbed system (up to 13 neighbor shells of the defect). We find that N defects have relatively the same change in in-plane and out-of-plane IFCs (N: $\Delta K_{ip} = 2.99\%$; $\Delta K_{op} = 2.98\%$), while B defects give larger percent change for the out-of-plane IFCs that govern ZA phonons (B: $\Delta K_{ip} = 3.31\%$; $\Delta K_{op} = 5.22\%$). For P defects, we also see $\Delta K_{ip} < \Delta K_{op}$ and $\tau_{ZA}^{-1} > \tau_{TA}^{-1} \approx \tau_{LA}^{-1}$, similar to B defects though larger (P: $\Delta K_{ip} = 5.29\%$; $\Delta K_{op} = 16.08\%$). However, mass variance also plays a significant role for in-plane scattering from P defects (Fig. 2c). The mass variance alone gives a percentage difference of the in-plane and out-of-plane components of the dynamical matrix of 7.04% and 6.09%, respectively. This explains the similarity between the yellow and black in-plane scattering rates in Fig. 2c.

Although the simple arguments just presented correlate with general features of the scattering rates, a single number cannot capture the complexity of the energy landscape created by the perturbation. Altering just a small number of IFCs among the thousands considered can lead to large variation in the scattering rates. For example, we find that replacing nine particular out-

of-plane IFCs near the N defect by the corresponding IFCs near the B defect (and re-enforcing the simple acoustic sum rule) makes $\tau_{Nitrogen}^{ZA} \approx \tau_{Boron}^{ZA}$ (Fig.3a). These "magic" IFCs were targeted because they present the largest opposing changes for the B and N defects (larger for B defects, smaller for N defects) with respect to the IFCs of perfect graphene. These out-of-plane IFCs are derived from interactions of first nearest neighbors of the defect with their second nearest neighbors (red lines in Fig. 3b). Moreover, our calculations show the lattice shrinks around a N defect and expands around B and P defects during relaxation (Fig. 3c). The opposing relaxation trends may be related to different IFC variations and radically different frequency trends seen for the scattering rates of ZA phonons in these systems. This suggests that the crystal structure local to the defect can play an important role in determining the behavior of phonon-defect scattering. As the scattering rates are built from variations of ~500 IFCs, elucidating a simple physical picture of the origins of the behaviors of the phonon-defect scattering rates beyond that presented here may not be possible. Perhaps further work with other defects and systems may better test these hypotheses.
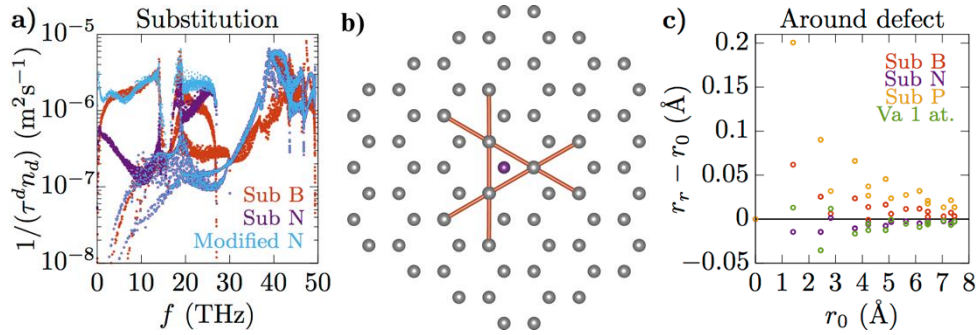

Figure 3. **a)** *T*-matrix scattering rates for a N substitution when the out-of-plane IFCs marked on **b)** are replaced by those for a B substitution (Modified N). Changing these IFCs recovers the ZA scattering rates of a B defect. **c)** Change in the distance between the defect and its nearest neighbor atoms after full relaxation (r_r) and before relaxation (r_0). This demonstrates that the lattice contracts around the N defect while it expands around the B and P defects.
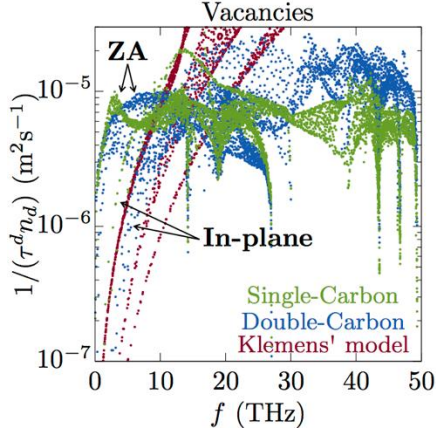
IV. PHONON-DEFECT SCATTERING BY VACANCIES

Figure 4. *T*-matrix phonon-defect scattering rates $(1/\tau_\lambda^d)$ of graphene with single- and double-Carbon vacancies. Note that these scattering rates are scaled to be independent of the arbitrary defect density n_d. As shown, the strength and frequency dependence of phonon-vacancy scattering rates drastically differ from the predictions of Klemens' effective mass defect model with $(\Delta m/m)^2 = 590$ [26].

Figure 4 gives the vacancy-scattering rates for single-Carbon and double-Carbon vacancies (two adjacent vacancies) in graphene calculated using the *T*-matrix method and compared with a modified Klemens' effective mass disorder model. Klemens' model considers a vacancy as a mass defect with a stronger mass variance $(\Delta m/m)^2 = 9$, to simulate the effects of broken bonds [11]. However, Fig. 4 shows the scattering resulting from a mass variance of 590, which was necessary to fit measurements of κ vs. vacancy density in graphene [26]. Even using this exaggerated $(\Delta m/m)^2$, the analytical model strongly underestimates (overestimates) the scattering rates for acoustic (optic) phonons as compared with those from the *T*-matrix methodology.   As the simple model neither captures the magnitude of the phonon-vacancy scattering nor the frequency dependence, key physics of this thermal resistance is missing from the effective mass approximation.

Note that the scattering rates due to single-Carbon vacancies in graphene are relatively frequency independent for much of the Brillouin zone (Fig. 4), suggesting that phenomenological models with weaker frequency dependence (e.g., $1/\tau^d \propto \omega^0$) would provide a better representation of this scattering mechanism over current analytical models that employ higher powers in the frequency dependence. Modeling vacancy-defect scattering with first order perturbation theory (Eq. 6) gives $1/\tau^d \propto \omega^2 D(\omega)$, and thus cannot capture the flat frequency trend obtained when IFC variance is included (Fig. 4). On the other hand, considering mass disorder only in the *T*-matrix calculations we find that the scattering rates smoothly flatten with frequency (become nearly independent of frequency) as the defect mass becomes large (Fig. 5). As the defect mass increases, the elements of the dynamical matrix related with the defect decrease ($\sim K_{i,j}/\sqrt{m_i m_j}$). This is equivalent to decreasing the IFCs related to the defect and in the limit of very large mass behaves as if the defect had no bonds with the atoms in the lattice. We note that this limit is not entirely equivalent to having a

Carbon vacancy for which the lattice locally relaxes and enforcement of the acoustic sum rule on the IFCs can play a significant role in determining the scattering rates (see Appendix B).
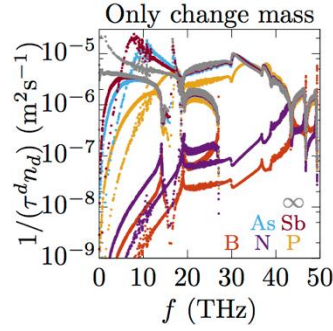

Figure 5. *T*-matrix scattering rates considering only changes of the defect mass. The masses are chosen as those of the elements that label each curve. The curve labeled ∞ represents $m = 10000$ amu. As the mass increases the slope of the ZA scattering rates smoothly transitions to that of a vacancy.

V.   PHONON-DEFECT SCATTERING AND THERMAL CONDUCTIVITY

The ultimate goal here for developing *ab initio* predictive calculations of phonon-defect scattering is to develop basic understanding of the role of defects on thermal conductivity of *real* materials, beyond perfect infinite crystals. The thermal conductivity of pristine graphene is very large κ ~2000-5000 W m^{-1} K^{-1} around room temperature [28,29,43–45], and ~75% of this is predicted to be carried by ZA phonons (for graphene of typical size ~10μm) [39]. Our Green's function calculations demonstrate that on-site mass (Eq. 6 Tamura [13]) and effective mass (Klemens [10,11]) defect models fail to capture the strength and frequency dependence of ZA phonon-defect scattering rates, therefore likely provide poor estimates of κ values in graphene with defects.

Ab initio calculations of graphene thermal conductivity as a function of defect concentration (Fig. 6a) show notable changes of κ for defect concentrations ~10^{-3}% ($n_d \approx 4 \times 10^{10}$ cm^{-2}). At that defect concentration κ decreases by 8.3%, 3.7%, 18%, 27% and 22% from that of pristine graphene for B, N and P substitutions and single-Carbon and double-Carbon vacancies, respectively. Changes in conductivity are negligible for defect concentrations ~10^{-4}% ($n_d \approx 4 \times 10^9$ cm^{-2}) and below.
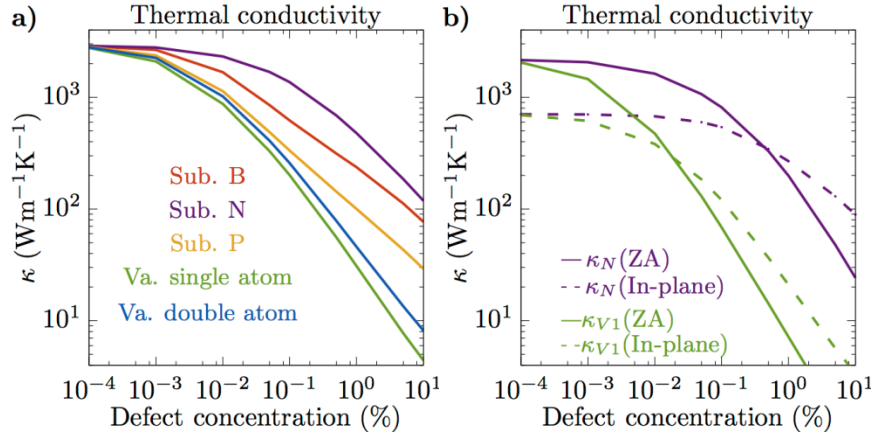
Figure 6. **a)** Calculated thermal conductivities vs. density for each defect type. Interestingly, the thermal conductivities of graphene with N substitutions and single-Carbon vacancies are larger than those with B substitutions and double-Carbon vacancies, respectively. **b)** Calculated thermal conductivities of graphene with N substitutions and single-Carbon vacancies by polarization: out-of-plane (ZA) (solid) and in-plane (dashed).

The behavior of the calculated κ of graphene with various defects derive from features of the ZA phonon-defect scattering rates. Figure 6a shows that the conductivity of graphene with N substitutions is twice that with B substitutions when the defect concentration is 0.1%. The larger conductivity follows from the order of magnitude weaker ZA scattering rates from N defects compared to those from B defects (Fig. 1). Figure 6a also shows that graphene with single-Carbon vacancies conducts heat better than its double-Carbon vacancies counterpart. We note that the double-Carbon vacancy has lower symmetry and significantly more variability with wave vector for the scattering rates than for the single vacancy (compare spread of rates in Fig. 9e to those in Fig. 9d). There is an interesting crossover of the out-of-plane and in-plane contributions to κ due to phonon-defect scattering (Fig. 6b) as the defect concentration increases. This follows from the relative strengths of the different scattering resistances for in-plane and out-of-plane (ZA) modes. While the intrinsic 3-phonon scattering resistance for ZA modes is smaller than for in-plane modes [39], the opposite is true for phonon-defect scattering rates (Fig. 1). Thus, as the defect concentration increases and the total scattering becomes dominated by phonon-defect processes, the ZA phonons scatter more strongly than the in-plane phonons and therefore contribute less to the total thermal conductivity.
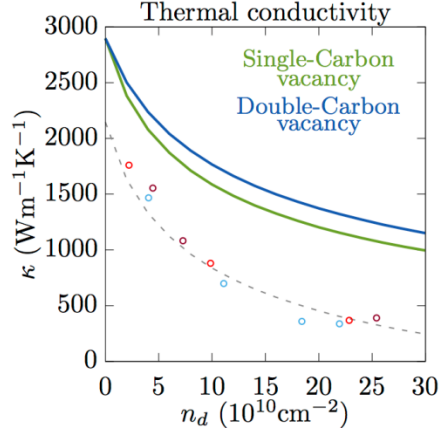
Figure 7. Calculated κ of graphene with vacancies vs. defect concentration compared with measured data (colored circles) [26]. Colors refer to specific samples where defects were introduced by irradiation from a low energy electron beam [26]. The dashed line is the calculated κ of graphene with single-Carbon vacancies shifted rigidly downwards by 750 W m^{-1} K^{-1} to highlight the similarities of the measured and calculated κ trends. The discrepancies between theory and experiment may arise from non-equilibrium effects leading to uncertainties in the extraction of κ from Raman spectroscopy signals, which are predicted to underestimate κ by a factor of 1.35 to 2.6 at room temperature [46].

The trend of κ vs. n_d obtained from our parameter-free calculations is very similar to that from experiment, though shifted above by ~750 W m^{-1} K^{-1} (Fig. 7). This rigid shift may be an artifact of the assumption of near thermal equilibrium of different phonon polarizations used in the procedure that relates Raman spectroscopy signals to thermal conductivity [46]. For graphene, calculations demonstrate that ZA phonons are strongly out-of-equilibrium during laser excitation and therefore room temperature κ measurements may be underestimated by a factor of 1.35 to 2.6 [46]. This is acknowledged by the authors of Ref. [26], who also claim that their study is focused on *relative* changes in thermal conductivity with defect density. Furthermore, the measured $\kappa \approx 1800$ W m^{-1} K^{-1} for the 'defect-free' graphene from CVD methods is comparable to measurements on similar samples, but substantially lower than measurements from exfoliation methods [28,47] and from values given here. This suggests that various extrinsic scattering mechanisms may be playing a significant role in determining κ, even before irradiation. Graphene from CVD methods might contain grain boundaries [48], polymer residue from nanofabrication [49], wrinkles [50], cracks [51] and possibly other defects. Those defects degrade κ and might also be related to the difference between our calculation and experimental data in Fig. 7. Given these arguments, the κ vs. n_d trends from calculation and measurement are reasonable.

VI.   SUMMARY AND CONCLUSIONS

We presented calculations of phonon-defect scattering rates due to B, N and P substitutions as well as single-Carbon and double-Carbon vacancies in graphene. Our parameter-free calculations are based on *ab initio* Green's function methods not restricted to small perturbations or low frequencies. These phonon-defect rates are coupled with the Peierls-Boltzmann transport equation to determine the effects of defects on phonon thermal conductivity in graphene. Our phonon-defect scattering results differ significantly from expectations derived from first order perturbation approaches, particularly when only considering mass variation. Structure and force variation near defects are found to be more important, particularly due to changes in interatomic force constants. We found that flexural acoustic (ZA) phonon scattering rates from N defects are nearly an order of magnitude smaller than those from B defects despite the mass difference between N and C being larger than that between B and C. Also, ZA scattering rates from N defects decreases with increasing frequency in the low frequency spectrum contrary to typical expectations for which rates increase as some power of the frequency. For Carbon vacancies in graphene, the ZA scattering rates are fairly independent of frequency for much of the spectrum. This suggests that phenomenological models may better represent this phenomena with scattering rates proportional to ω^0. Furthermore, our parameter-free calculations compare favorably with the trend of thermal conductivity with defect density from measurements, though miss the overall magnitudes observed. We discussed these unusual phonon-defect scattering features in terms of structure, force and mass variations and connected these with thermal transport. Furthermore, we demonstrated that on-site mass and effective mass defect models fail to capture the strength and frequency dependence of ZA phonon-defect scattering rates, therefore likely provide poor estimates of κ values in graphene with defects. This work provides benchmark calculations for models of point defect scattering in graphene, and demonstrates the utility of *ab initio* methods for modeling thermal transport in materials with defects.

VII. ACKNOWLEDGEMENTS

APPENDIX A: SIMULATION DETAILS

Density functional theory (DFT) details: Energies and interatomic forces were determined using the module pw.x of Quantum Espresso (QE) [52], a plane wave based density functional theory software package. For each self-consistent field computation, we used norm conserving pseudopotentials within the local density approximation and Perdew-Zunger

parametrization [53]; a cut-off energy of 100 Ry; an electronic convergence threshold of 10^{-10} Ry; Marzari-Vanderbilt smearing [52] with gaussian spread of 0.02 Ry and a vacuum distance between graphene planes of 29 Å . Energy minimization in defect-free graphene gives a lattice constant $a = 2.441$ Å. Harmonic interatomic force constants (IFCs) were determined from finite displacements (± 0.04 Å) of atoms in 9×9 supercells of the primitive two-Carbon unit cell sampling only the Γ point of the Brillouin zone. The IFCs were considered up to the 13th nearest neighbor shell. On those IFCs, we enforce the space group symmetries and translational invariance using singular value decomposition and quadratic programming [54]. Our IFCs agree well with previous calculations [39] and give reasonable agreement with measured phonon dispersion data, especially for heat-carrying acoustic modes (Fig. 8).
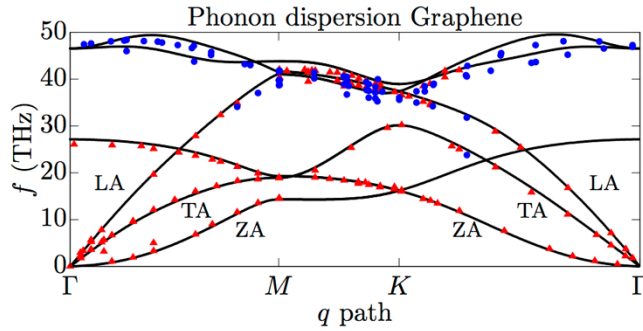

Figure 8. Calculated phonon dispersion of graphene (solid curves). Dots [55] and triangles [56] are from inelastic x-ray scattering measurements on in-plane graphite. Due to the weak coupling between layers, the in-plane dispersion of graphite and graphene are similar.

Graphene with defects: Each defect is put at the center of the 9×9 supercell, which is then further relaxed using the pw.x module of QE while keeping the volume of the supercell fixed until the interatomic forces are less than 10^{-5} Ry/Bohr. To accelerate the relaxation, the atomic masses were decreased following the procedure outlined in the documentation of the Car-Parrinello package within Quantum Espresso. At the end of that process, the atomic masses were increased to ~50 amu to obtain fine tuning of the relaxed atomic positions and enhanced minimization of the interatomic forces. For all defects, the initial graphene sheet was assumed flat and after relaxing all atomic positions in every direction it remained flat. Relaxed distances between defects and their six nearest neighbor shells are summarized in Table I. These results are consistent with previous DFT calculations in like systems [57–60]. Note that the lattice expands around the B and P defect while it contracts around the N defect. The symmetry of each supercell with a defect was found using the spglib library created by A. Togo. Each single-atom defect has P-6m2 (187) symmetry, while the double-Carbon vacancy (two adjacent vacancies) has Cmmm (65) symmetry.

	d-C_1 (Å)	d-C_2 (Å)	d-C_3 (Å)	d-C_4 (Å)	d-C_5 (Å)	d-C_6 (Å)
None	1.409	2.441	2.818	3.728	4.227	4.881
B	1.471	2.466	2.824	3.751	4.241	4.898
N	1.395	2.426	2.819	3.718	4.223	4.874
P	1.610	2.531	2.849	3.794	4.264	4.927

V	1.422	2.405	2.830	3.712	4.215	4.869

Table I. Distances between the center of each single-atom defect and atoms in six nearest neighbor shells. The distances are the same for all atoms in a particular neighbor shell. The first row corresponds to a perfect graphene lattice.

After relaxation, the IFCs were determined using the same procedures outlined above (symmetries enforced, displacements, etc.). Then, we replace the defect mass and the IFCs between atomic pairs within the 13 nearest neighbor shells of the defect on the central region of a larger rectangular supercell (240 atoms) of perfect graphene. The rectangular shape facilitates the set-up of the Green's function calculations. We neglect IFCs relating atoms beyond the 13 neighbor shells. The size of the supercell guarantees that the Carbon atoms on the edges of the supercell have interactions equal to those of Carbon atoms in bulk graphene. Finally, we enforce the simple acoustic sum rule, which reduces the symmetry of the onsite IFC matrices of atoms close to the defect (Appendix B).

Green's function scattering rates: IFCs of the modified rectangular supercell define the dynamical matrix of the system with defects H_d, while those from the unmodified rectangular supercell define the dynamical matrix of the unperturbed system H_0 with their difference giving the perturbation $V_d = H_d - H_0$ in Eq. 3. To calculate the Green's function of the unmodified supercell G_0, also in Eq. 3, we follow the approach described by Mingo et al. [15]. That is, G_0 is determined on a combined reciprocal and real space coordinate system and then transformed to real space. All integrations employed 200 grid points in reciprocal space. Finally, the *T*-matrix and scattering rates were obtained using the equations in Sec. II. Calculated phonon-defect scattering rates for different defects are shown in Fig. 9, where we also highlight the contribution from the different polarizations. Recall that most of the heat in graphene is carried by the ZA phonons and thus ZA phonon-defect scattering governs the changes in thermal conductivity due to point defects.
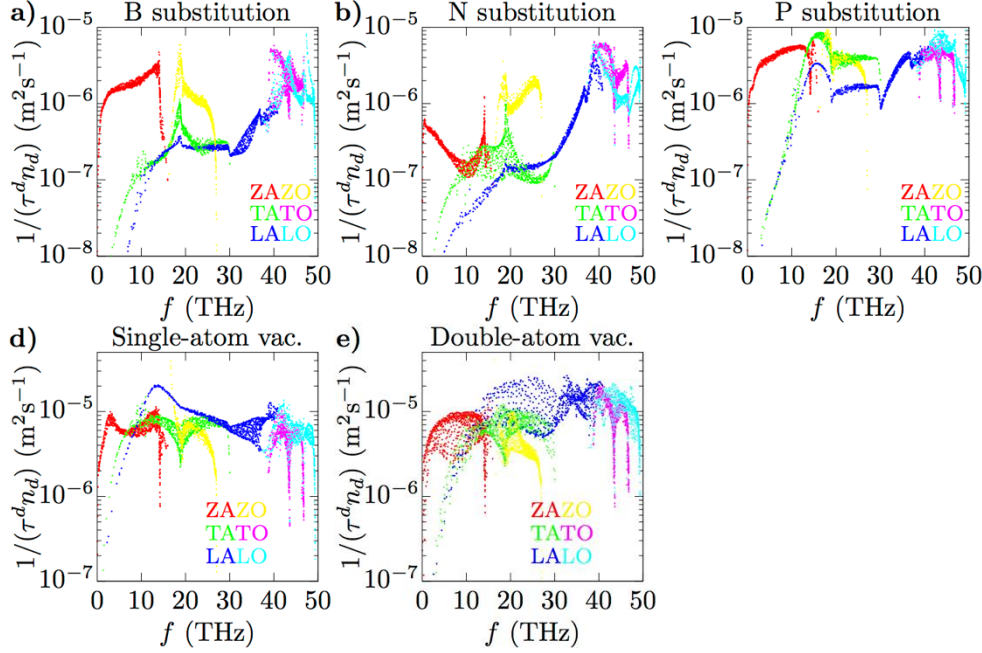
Figure 9. *T*-matrix scattering rates for B, N and P substitutions as well as single-Carbon and double-Carbon vacancies in graphene, colored according to polarization.

Thermal conductivity calculations: κ for graphene with defects is calculated as described in Section II including thermal resistance from point defects, isotope variation, boundaries and intrinsic three-phonon scatterings. Phonon-defect scattering rates are defined in great detail above, while phonon-isotope scattering rates are given by Eq. 6 using natural Carbon isotope concentrations (1.1% ^{13}C, 98.9% ^{12}C). An empirical phonon-boundary scattering rate for each mode is given by $1/\tau_\lambda^b = |v_\lambda|/L$ [36] where $L = 7.5\mu m$, chosen to match graphene systems in Ref. [26]. These are all combined with the rates for scatterings of three phonons (lowest order in perturbation theory) which build the right-hand side of the steady-state linearized Peierls-Boltzmann transport equation [36,38,39]

$$
(7) \quad k_B T \, \vec{v}_\lambda \cdot \vec{\nabla} T \frac{\partial n_\lambda^0}{\partial T}
$$
$$
= \sum_{\lambda'\lambda''} \left[W_{\lambda\lambda'\lambda''}^+ (\Omega_{\lambda''} - \Omega_{\lambda'} - \Omega_\lambda) + \frac{1}{2} W_{\lambda\lambda'\lambda''}^- (\Omega_{\lambda''} + \Omega_{\lambda'} - \Omega_\lambda) \right] - \frac{n_\lambda^0(n_\lambda^0 + 1)\Omega_\lambda}{\tau_\lambda^b}
$$
$$
- \frac{n_\lambda^0(n_\lambda^0 + 1)\Omega_\lambda}{\tau_\lambda^d}
$$

with $W_{\lambda\lambda'\lambda''}^+$ and $W_{\lambda\lambda'\lambda''}^-$ from three-phonon scattering processes defined in Ref. 1. Phonon-defect scattering is included in Eq. 7 similar to that of phonon-boundary scattering [39], and

they do not depend on the distribution of modes λ' and λ''. This equation is solved iteratively [35] for the deviations from equilibrium Ω_λ for each phonon mode, which determine the transport lifetimes in Eq. 4, $\tau_{\lambda\alpha} = \Omega_\lambda T / \hbar \omega_\lambda v_{\lambda\alpha}$. Construction and solution of Eq. 7 for graphene has been discussed in detail in previous work [39,40]. The procedures and details for determining harmonic and third-order anharmonic IFCs (only inputs to the calculations) are similar to those described above for the Green's function calculations with some minor exceptions: (i) anharmonic IFCs were considered to the fifth nearest neighbor shell only [39], (ii) point group symmetries and translational invariance were enforced with a χ^2 minimization procedure [5,39], and (iii) additional equilibrium invariance constraints described by Born and Huang [61,62] were applied to the harmonic IFCs.

APPENDIX B: BENCHMARKING

To benchmark our numerical algorithms for phonon-defect scattering rates, we compare the phonon-isotope scattering rates of graphene calculated from the Green's function approach with those from Tamura's first order perturbation approximation (Eq. 6). For small mass change, the two methods generally agree when only changes in the atomic masses are considered– no force variance: Fig. 10a for isotope variation and Fig. 10b and Fig. 10c for Boron and Nitrogen substitutions. However, for larger mass impurities the deviations are significant (Fig. 10d and Fig. 5). For the P substitution, the scattering of high frequency phonons is overestimated by more than an order of magnitude by Tamura's expression, as the qualitative frequency trends given by each method are quite different. The Green's function calculation gives a crossover between the ZA and TA rates and also gives $\tau_{ZO}^{-1} < \tau_{LA}^{-1}$. These features are not captured by Tamura's approximation because changing the mass mostly changes g in Eq. 6 while intrinsic phonon properties (e.g., frequencies, velocities) change very little for reasonable defect concentrations. Thus, as the mass increases, the scattering rates from Tamura's approximation simply shift upwards.
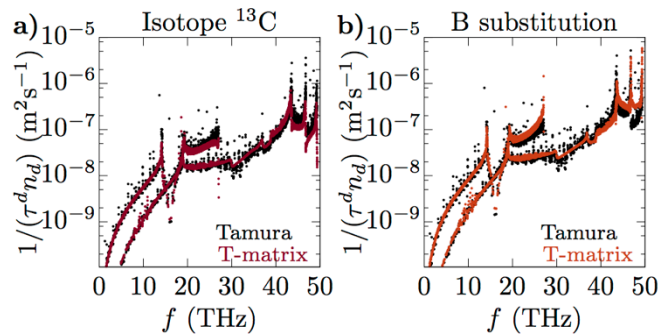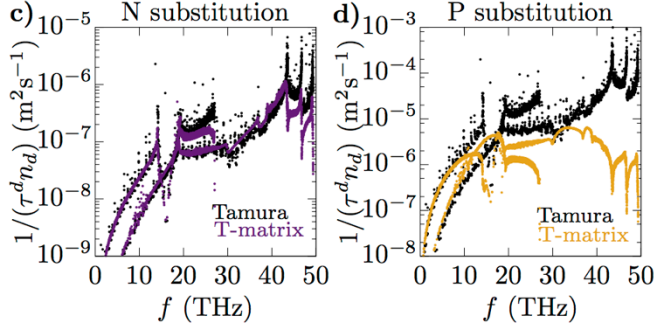
Figure 10. Scattering rates from the *T*-matrix method compared with Tamura's first order perturbation approximation (Eq. 6) when only the atomic mass is varied for **a)** ^{13}C isotopes, **b)** B, **c)** N and **d)** P substitutions.

We also tested the convergence of our scattering rates with respect to the size of the neighborhood around the defect for which IFC variance was considered (Fig. 11). Our results indicate that including variation up to the 5th neighbor shell around the defect gives a good approximation for all the defects except for the N substitution, for which inclusion of up to the 9th neighbor shell was required for reasonable convergence. The largest differences between the rates happen in the low frequency spectrum, likely a consequence of enforcing the simple acoustic sum rule (ASR). As the number of shells decreases, the acoustic sum rule worsens and we need to impose a larger change to the onsite IFCs of the atoms around the defect. This change affects mostly the low frequency spectrum.
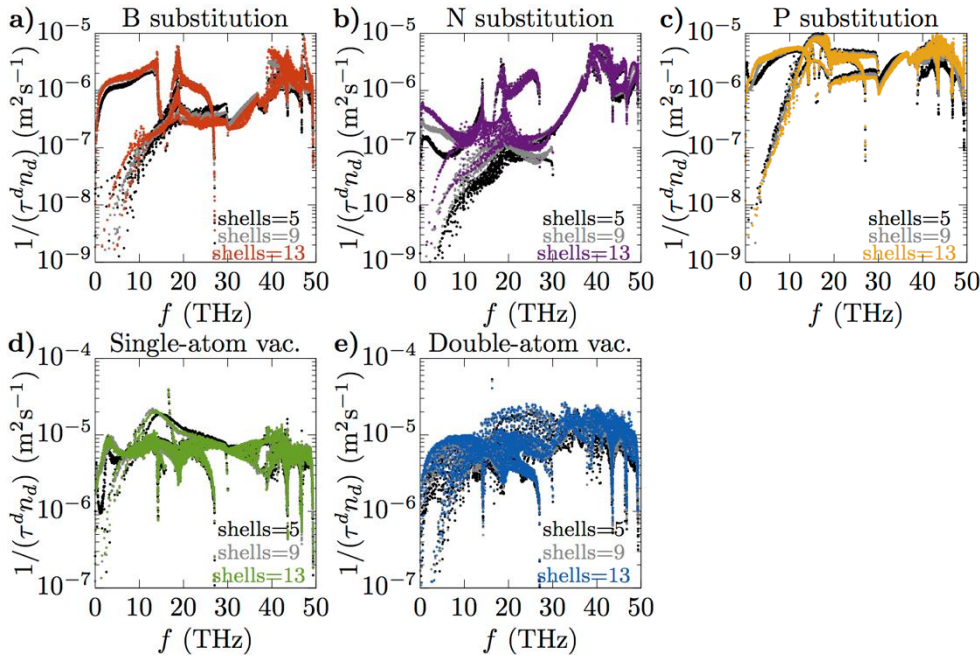
Figure 11. Scattering rates from the *T*-matrix method as the number of nearest neighbor shells for which the defect induced IFC changes is varied.

Enforcing the ASR is necessary to properly capture the low frequency behavior of the scattering rates. After construction, the set of IFCs of the rectangular supercell (used for the Green's function calculations) does not satisfy the ASR. This happens because for each atom except the defect, the IFCs of at least one shell are an uneven combination of IFCs from perfect graphene with IFCs from the relaxed supercell. Nevertheless, the IFCs of atoms close to the defect almost satisfy the ASR because they mostly come from IFCs of the fully relaxed 9×9 supercell, while the IFCs of atoms away from the defect (shell 13 of the defect) almost satisfy the ASR because they mostly come from IFCs of perfect graphene. Therefore, we enforce only a simple ASR. Failing to enforce it causes divergent behavior of the scattering rates at low frequencies (Fig. 12a). For unrelaxed graphene with a vacancy, where only the IFCs related to the vacancies are eliminated, not enforcing the ASR has much more significant consequences (Fig. 12b). Note that the scattering rates of the unrelaxed vacancy without enforcing ASR (Fig. 12b) are equivalent to those of a substitution with infinite mass (Fig. 5).
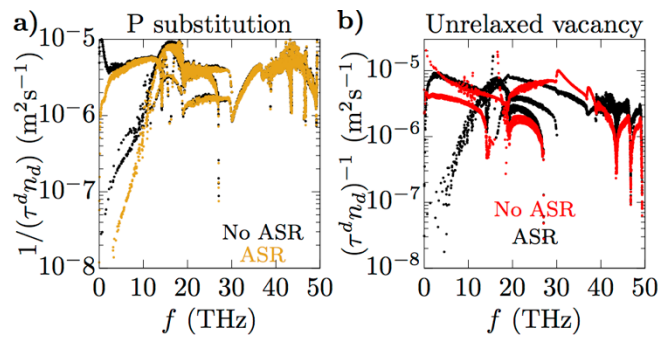

Figure 12. *T*-matrix scattering rates when the acoustic sum rule (ASR) is enforced and not enforced for a P substitution **(a)** and for a single-Carbon vacancy **(b)** where only the IFCs related to the defect are eliminated but the system is not relaxed.

Relaxation of the defects and computation of the IFCs from density functional theory supercell calculations can be computationally expensive, ~15k cpu hours for each 162 atom supercell calculation. System relaxation for the N, B and P defect structures plays a significant role in determining phonon-defect scattering rates (Fig. 2); however, phonon-vacancy scattering rates from the *T*-matrix formalism are fairly well captured without the full relaxation of the system (Fig. 13). Thus, for vacancies in graphene significant computational costs can be saved, while providing a better representation of the magnitude and frequency dependence of phonon-vacancy scattering over simple analytical models (Fig. 4). Note that the unrelaxed structure gives a fair description of the ZA phonon-vacancy scattering rates and thermal conductivity at

low defect concentrations, where the ZA phonons carry most of the heat. For instance, at 0.01% vacancy concentration ($n_d \approx 4 \times 10^{11}$ cm^{-2}) the approximated κ is about 10% larger than for the fully relaxed structure at room temperature.
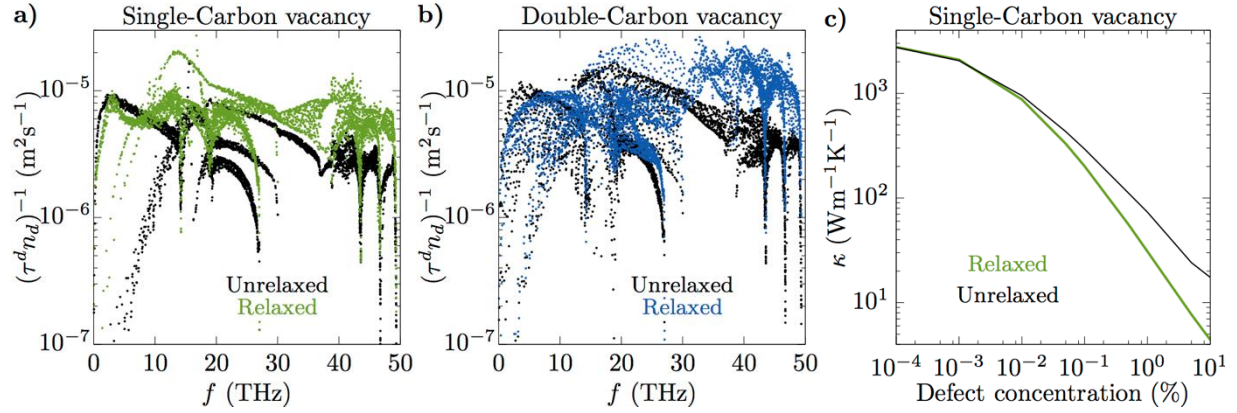

Figure 13. *T*-matrix scattering rates for **a)** single-Carbon and **b)** double-Carbon vacancies in graphene comparing unrelaxed and fully relaxed rates. For the unrelaxed system, only the IFCs related to the vacancies are eliminated and the simple acoustic sum rule enforced. The approximation fairly well captures the scattering rates from the full calculation, while saving ~15k cpu hours (162 atom supercell). c) Thermal conductivity of graphene with single-Carbon vacancies comparing results for fully relaxed and unrelaxed systems.

References

[1]   D. A. Broido, M. Malorny, G. Birner, N. Mingo, and D. A. Stewart, Appl. Phys. Lett. **91**, 231922 (2007).

[2]   A. Ward, D. A. Broido, D. A. Stewart, and G. Deinzer, Phys. Rev. B **80**, 125203 (2009).

[3]   K. Esfarjani, G. Chen, and H. T. Stokes, Phys. Rev. B **84**, 85204 (2011).

[4]   L. Lindsay, Nanoscale Microscale Thermophys. Eng. **20**, 67 (2016).

[5]   N. Mingo, D. A. Stewart, D. A. Broido, L. Lindsay, and W. Li, in *Length-Scale Depend. Phonon Interact.*, edited by S. L. Shindé and G. P. Srivastava (Springer New York, New York, NY, 2014), pp. 137--173.

[6]   L. Lindsay, D. A. Broido, and T. L. Reinecke, Phys. Rev. Lett. **111**, 25901 (2013).

[7]   B. Lv, Y. Lan, X. Wang, Q. Zhang, Y. Hu, A. J. Jacobson, D. Broido, G. Chen, Z. Ren, and C.-W. Chu, Appl. Phys. Lett. **106**, 74105 (2015).

[8]   J. Kim, D. A. Evans, D. P. Sellan, O. M. Williams, E. Ou, A. H. Cowley, and L. Shi, Appl. Phys. Lett. **108**, 201905 (2016).

[9]   N. H. Protik, J. Carrete, N. A. Katcho, N. Mingo, and D. Broido, Phys. Rev. B **94**, 45207 (2016).

[10]   P. G. Klemens, Proc. Phys. Soc. Sect. A **68**, 1113 (1955).

[11]   C. A. Ratsifaritana and P. G. Klemens, Int. J. Thermophys. **8**, 737 (1987).

[12]   A. AlShaikhi, S. Barman, and G. P. Srivastava, Phys. Rev. B **81**, 195320 (2010).

[13]   S. Tamura, Phys. Rev. B **27**, 858 (1983).

[14]   L. Lindsay, D. A. Broido, and T. L. Reinecke, Phys. Rev. B **88**, 144306 (2013).

[15]   N. Mingo, K. Esfarjani, D. A. Broido, and D. A. Stewart, Phys. Rev. B **81**, 45408 (2010).

[16]   A. Kundu, N. Mingo, D. A. Broido, and D. A. Stewart, Phys. Rev. B **84**, 125426 (2011).

[17]   P. Chen, N. A. Katcho, J. P. Feser, W. Li, M. Glaser, O. G. Schmidt, D. G. Cahill, N. Mingo, and A. Rastelli, Phys. Rev. Lett. **111**, 115901 (2013).

[18]   N. A. Katcho, J. Carrete, W. Li, and N. Mingo, Phys. Rev. B **90**, 94117 (2014).

[19]   T. Wang, J. Carrete, A. van Roekeghem, N. Mingo, and G. K. H. Madsen, Phys. Rev. B **95**, 245304 (2017).

[20]   A. K. Geim and K. S. Novoselov, Nat Mater **6**, 183 (2007).

[21]   A. K. Geim, Science (80-.). **324**, 1530 LP (2009).

[22]   L. G. Cançado, A. Jorio, E. H. M. Ferreira, F. Stavale, C. A. Achete, R. B. Capaz, M. V. O. Moutinho, A. Lombardo, T. S. Kulmala, and A. C. Ferrari, Nano Lett. **11**, 3190 (2011).

[23]   A. Eckmann, A. Felten, A. Mishchenko, L. Britnell, R. Krupke, K. S. Novoselov, and C. Casiraghi, Nano Lett. **12**, 3925 (2012).

[24]   L. S. Panchakarla, K. S. Subrahmanyam, S. K. Saha, A. Govindaraj, H. R. Krishnamurthy, U. V Waghmare, and C. N. R. Rao, Adv. Mater. **21**, 4726 (2009).

[25]   L. Zhao, R. He, K. T. Rim, T. Schiros, K. S. Kim, H. Zhou, C. Gutiérrez, S. P. Chockalingam, C. J. Arguello, L. Pálová, D. Nordlund, M. S. Hybertsen, D. R. Reichman, T. F. Heinz, P. Kim, A. Pinczuk, G. W. Flynn, and A. N. Pasupathy, Science (80-.). **333**, 999 (2011).

[26]   H. Malekpour, P. Ramnani, S. Srinivasan, G. Balasubramanian, D. L. Nika, A. Mulchandani, R. K. Lake, and A. A. Balandin, Nanoscale **8**, 14608 (2016).

[27]   F. Banhart, J. Kotakoski, and A. V. Krasheninnikov, ACS Nano **5**, 26 (2011).

[28]   A. A. Balandin, S. Ghosh, W. Bao, I. Calizo, D. Teweldebrhan, F. Miao, and C. N. Lau, Nano Lett. **8**, 902 (2008).

[29]   W. Cai, A. L. Moore, Y. Zhu, X. Li, S. Chen, L. Shi, and R. S. Ruoff, Nano Lett. **10**, 1645 (2010).

[30]   C. Faugeras, B. Faugeras, M. Orlita, M. Potemski, R. R. Nair, and A. K. Geim, ACS Nano **4**, 1889 (2010).

[31] A. A. Balandin, Nat. Mater. **10**, 569 (2011).

[32] D. L. N. and A. A. Balandin, Reports Prog. Phys. **80**, 36502 (2017).

[33] N. Mingo and L. Yang, Phys. Rev. B **68**, 245406 (2003).

[34] J.-S. Wang, J. Wang, and J. T. Lü, Eur. Phys. J. B **62**, 381 (2008).

[35] M. Omini and A. Sparavigna, Phys. Rev. B **53**, 9064 (1996).

[36] J. M. (John M. . Ziman, *Electrons and Phonons : The Theory of Transport Phenomena in Solids* (Clarendon Press, 2001).

[37] G. Fugallo, M. Lazzeri, L. Paulatto, and F. Mauri, Phys. Rev. B **88**, 45430 (2013).

[38] G. Srivastava, *The Physics of Phonons* (Taylor & Francis Group, New York, NY, 1990).

[39] L. Lindsay, W. Li, J. Carrete, N. Mingo, D. A. Broido, and T. L. Reinecke, Phys. Rev. B **89**, 155426 (2014).

[40] L. Lindsay, D. A. Broido, and N. Mingo, Phys. Rev. B **82**, 115427 (2010).

[41] S. Lee, D. Broido, K. Esfarjani, and G. Chen, Nat. Commun. **6**, 6290 (2015).

[42] A. Cepellotti, G. Fugallo, L. Paulatto, M. Lazzeri, F. Mauri, and N. Marzari, Nat. Commun. **6**, 6400 (2015).

[43] S. Chen, A. L. Moore, W. Cai, J. W. Suk, J. An, C. Mishra, C. Amos, C. W. Magnuson, J. Kang, L. Shi, and R. S. Ruoff, ACS Nano **5**, 321 (2011).

[44] J.-U. Lee, D. Yoon, H. Kim, S. W. Lee, and H. Cheong, Phys. Rev. B **83**, 81419 (2011).

[45] S. Chen, Q. Wu, C. Mishra, J. Kang, H. Zhang, K. Cho, W. Cai, A. A. Balandin, and R. S. Ruoff, Nat. Mater. **11**, 203 (2012).

[46] A. K. Vallabhaneni, D. Singh, H. Bao, J. Murthy, and X. Ruan, Phys. Rev. B **93**, 125432 (2016).

[47] S. Ghosh, I. Calizo, D. Teweldebrhan, E. P. Pokatilov, D. L. Nika, A. A. Balandin, W. Bao, F. Miao, and C. N. Lau, Appl. Phys. Lett. **92**, 151911 (2008).

[48] A. Y. Serov, Z.-Y. Ong, and E. Pop, Appl. Phys. Lett. **102**, 33104 (2013).

[49] M. T. Pettes, I. Jo, Z. Yao, and L. Shi, Nano Lett. **11**, 1195 (2011).

[50] Y. Zhang, T. Gao, Y. Gao, S. Xie, Q. Ji, K. Yan, H. Peng, and Z. Liu, ACS Nano **5**, 4014 (2011).

[51] I. Wlasny, P. Dabrowski, M. Rogala, P. J. Kowalczyk, I. Pasternak, W. Strupinski, J. M. Baranowski, and Z. Klusek, Appl. Phys. Lett. **102**, 111601 (2013).

[52] P. Giannozzi, S. Baroni, N. Bonini, M. Calandra, R. Car, C. Cavazzoni, D. Ceresoli, G. L. Chiarotti, M. Cococcioni, I. Dabo, A. D. Corso, S. de Gironcoli, S. Fabris, G. Fratesi, R. Gebauer, U. Gerstmann, C. Gougoussis, A. Kokalj, M. Lazzeri, L. Martin-Samos, N. Marzari, F. Mauri, R. Mazzarello, S. Paolini, A. Pasquarello, L. Paulatto, C. Sbraccia, S. Scandolo, G. Sclauzero, A. P. Seitsonen, A. Smogunov, P. Umari, and R. M. Wentzcovitch, J. Phys. Condens. Matter **21**, 395502 (2009).

[53] J. P. Perdew and A. Zunger, Phys. Rev. B **23**, 5048 (1981).

[54] K. Esfarjani and H. T. Stokes, Phys. Rev. B **77**, 144112 (2008).

[55] J. Maultzsch, S. Reich, C. Thomsen, H. Requardt, and P. Ordej'on, Phys. Rev. Lett. **92**, 75501 (2004).

[56] M. Mohr, J. Maultzsch, E. Dobard\ifmmode z\else z\fii\ifmmode c\else c\fi, S. Reich, I. Milo\ifmmode s\else s\fievi\ifmmode c\else c\fi, M. Damnjanovi\ifmmode c\else c\fi, A. Bosak, M. Krisch, and C. Thomsen, Phys. Rev. B **76**, 35439 (2007).

[57] J. Dai, J. Yuan, and P. Giannozzi, Appl. Phys. Lett. **95**, 232105 (2009).

[58] M. Wu, C. Cao, and J. Z. Jiang, Nanotechnology **21**, 505202 (2010).

[59]   N. Al-Aqtash, K. M. Al-Tarawneh, T. Tawalbeh, and I. Vasiliev, J. Appl. Phys. **112**, 34304 (2012).

[60]   H. R. Jiang, T. S. Zhao, L. Shi, P. Tan, and L. An, J. Phys. Chem. C **120**, 6612 (2016).

[61]   M. Born and K. Huang, *Dynamical Theory of Crystal Lattices* (Clarendon Press, Oxford, 1998).

[62]   L. Lindsay and Y. Kuang, Phys. Rev. B **95**, 121404 (2017).